Electronic Supplementary Material (ESI) for New Journal of Chemistry.

Supporting Information

Polyoxometalate-based Composite Cluster with Core-Shell Structure: $Co_4(PW_9)_2$@Graphdiyne as Stable Electrocatalyst for Oxygen Evolution and its Mechanism Research

Hao Sun,[a] Chaojun Jing,*[a] Wenhui Shang,[a] Fei Wang, [a] Muling Zeng,[c] Shijie Ju,[c] Kai Li,*[b] Zhiyu Jia*[a]

[a] MOE Key Laboratory of Cluster Science, Key Laboratory of Photoelectronic /Electrophotonic Conversion Materials, School of Chemistry and Chemical Engineering, Beijing Institute of Technology, Beijing 100081, P. R. China. E-mail: jzy@bit.edu.cn, jingcj@bit.edu.cn.

[b] State Key Laboratory of Rare Earth Resource Utilization, Changchun Institute of Applied Chemistry, Chinese Academy of Sciences, Changchun 130022, P. R. China. E-mail: likai@ciac.ac.cn.

[c] School of Biotechnology and Health Sciences, Wuyi University, Jiangmen 529020, P. R. China.

1. Equipment, chemicals and reaction conditions

Single crystal X-ray diffraction of $Co_4(PW_9)_2$ microcrystal data was obtained by Bruker D8 Venture X-ray diffraction.

Scanning electron microscopy (SEM) images and **energy dispersive X-ray spectroscopy (EDS)** data were obtained through Zeiss Supra 55 SAPPHIRE SEM equipment with an EDS detector.

Transmission electron microscopy (TEM) and **high-resolution transmission electron microscopy (HRTEM)** images and corresponding **element mapping** were acquired by JEOL JEM-2100F transmission electron microscope

Powder X-ray diffraction (PXRD) data were detected on a Rigaku XRD-6000 diffractometer under the following conditions: 40 kV, 40 mA, Cu Kα radiation (λ = 0.154 nm).

Raman spectroscopy is recorded on a Renishaw Raman spectrometer at a laser excitation wavelength of 532 nm.

X-ray photoelectron spectroscopy (XPS) plots are obtained by monochromatized Al Kα exciting X-radiation (PHI Quantera SXM).

Electrochemical techniques are carried out on a CH instruments CHI 760E electrochemical workstation with a standard three-electrode cell, where $Co_4(PW_9)_2$@GDY as the working electrode, graphite rod as the counter electrode and saturated calomel electrode (SCE) as the reference electrode.

Thermogravimetric Analysis (TGA) data was acquired using a TG/DSC 1/1100 SF from METTLER TOLEDO under N_2 flow at a heating rate of 10 $^{\circ}C\ min^{-1}$.

Thin layer chromatography (TLC) was performed using Merck aluminium-backed plates of TLC Silica gel 60 F_{254}; the plates were revealed using UV light.

Column chromatography was accomplished using silica gel (60 Å pore size, 230-400 μm mesh size).

Nuclear Magnetic Resonance (NMR) Spectrum were recorded using Bruker Avance 400 spectrometers (Analysis & Testing Center, Beijing Institute of Technology).

Reagents and chemicals are used as received without further purification. Dichloromethane and diethyl ether were used as received. Tetrahydrofuran was dried by passing through a column of activated molecular sieves using a solvent purification system. All water used was purified with a Millipore system (typically 18.2 MΩ cm resistivity).

Reaction conditions was conducted under inert atmosphere by nitrogen when using a standard Schlenk line technique. All other reactions were performed employing standard organic synthesis protocols.

2. Synthetic procedures

2.1 Preparation of $Co_4(PW_9)_2$ microcrystal

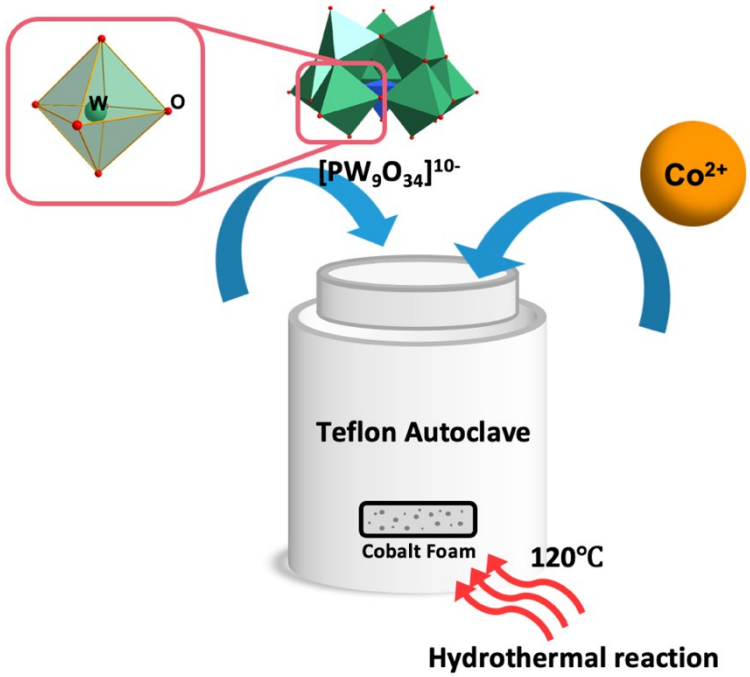

Fig. S1. Illustration of preparing $Co_4(PW_9)_2$ microcrystal under hydrothermal reaction

$Co(NO_3)_2 \cdot 6H_2O$ (0.2 mmol), $Na_9[A\text{-}\alpha\text{-}PW_9O_{34}] \cdot 7H_2O$ (0.1 mmol) and KCl (1.00 mmol) were mixed in deionized H_2O (10 mL) in a 25 mL Teflon autoclave and stirring for half an hour, then the pH value of the mixture was adjusted to 7.5 by 1M HCl and 1M NaOH. Teflon autoclave was then heated to 120 °C for 6 h and cooling successively in room temperature and 4 °C overnight. The amount of KCl and suitable pH are discussed at large in Fig. S2 and S3.

2.2 Synthesis of hexakis[(trimethylsilyl)ethynyl]benzene (HEB-TMS).

HEB-TMS as the precursor of all-carbon GDY was synthesized according to the reported route shown in Scheme. S1.[1] First, 20 mL anhydrous THF and 4.24 mL trimethylsilylacetylene (30 mmol) was added to N_2-filled Schlenk flask which was put into -78 °C condition, then 2.51 mL n-BuLi (30 mmol) was added dropwise into the mixture and stirred for 1 h. Second, 4.0894g $ZnCl_2$ (30 mmol) was added into the reacted solution and stirred for 3 h, the low temperature condition was removed at same time to bring the reaction temperature back to the room temperature, [(trimethylsilyl)ethynyl]zinc chloride was obtained when the reaction completed.[2] Third, 2.7574g hexabromobenzene (5 mmol), 1.1556g $Pd(PPh_3)_4$ (1 mmol) and 20 mL anhydrous toluene were added, then the mixture was stirred at 80 °C for 72 h under N_2 atmosphere. Finally, after 30 mL 1 M HCl was added to the reaction, the mixture was extracted with ethyl acetate for three times, and the organic phase was collected and washed with brine and dried with anhydrous $MgSO_4$, then dried organic phase was evaporated, and the residue was purified by column chromatography with silica gel (petroleum ether as eluent). HEB-TMS was separated as pale-yellow powder, the ^1H NMR and ^{13}C NMR of HEB-TMS were shown in Fig. S4 and Fig. S5. ^1H NMR (400 MHz, $CDCl_3$) δ 0.12 (s, 54H). ^{13}C NMR (101 MHz, $CDCl_3$) δ 127.95 (C=C), 105.19 (C≡C), 100.99 (C-Si), 0.28 (Si-CH_3).

2.3 Synthesis of $Co_4(PW_9)_2$@GDY electrode.

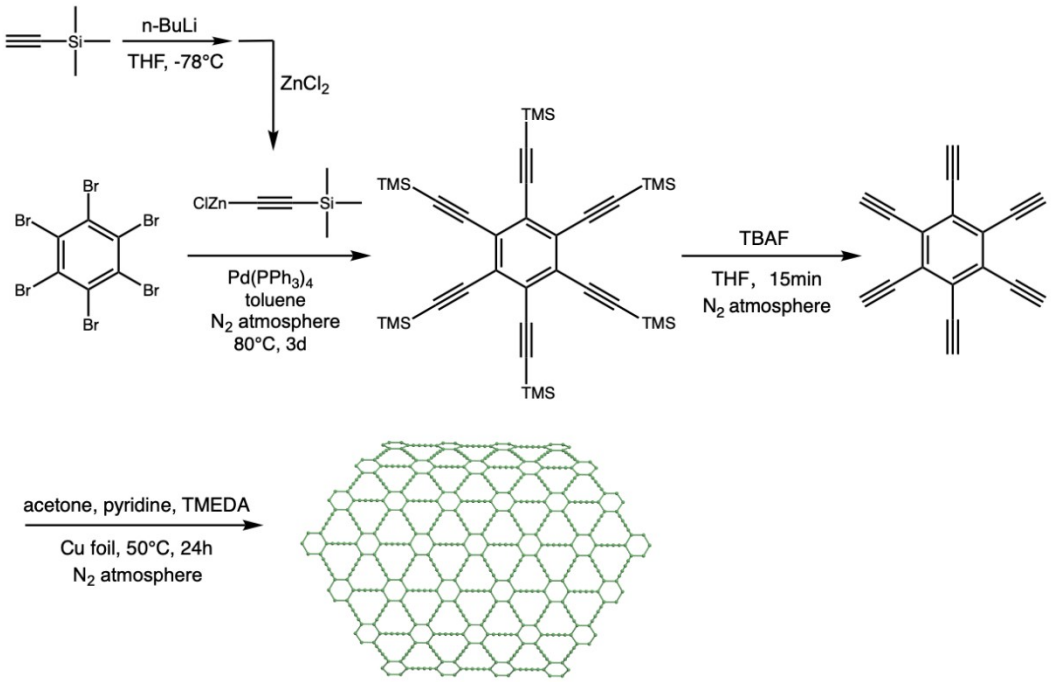

Scheme S1. The synthesis route for GDY

3. Results and Discussion

3.1 Favorable pH value for preparation $Co_4(PW_9)_2$ microcrystal and correspond SEM images

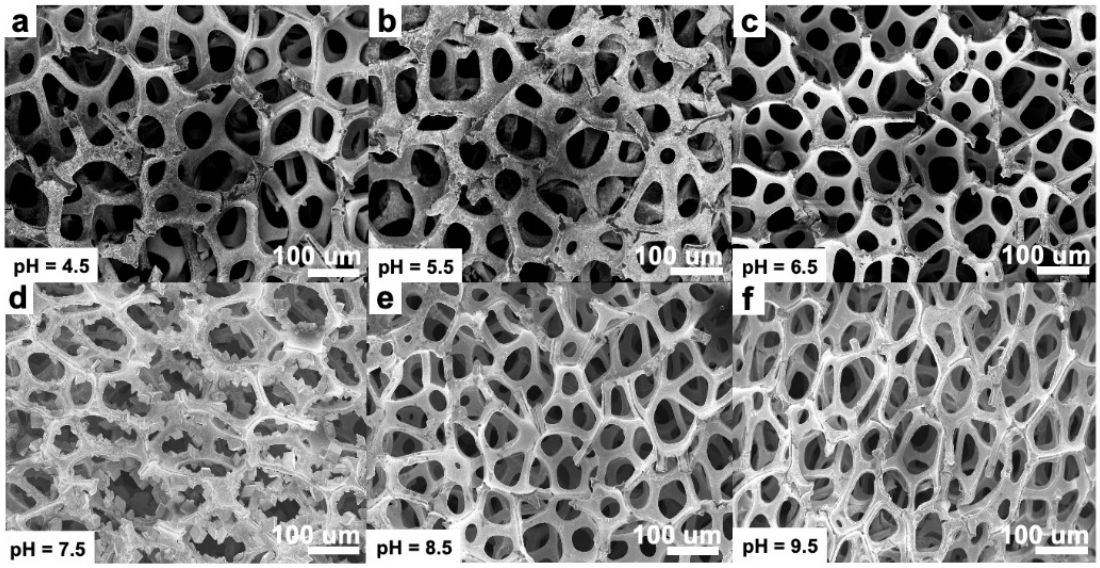

Fig. S2. The SEM images of preparation $Co_4(PW_9)_2$ microcrystal under different pH conditions

$Co(NO_3)_2 \cdot 6H_2O$ (0.2 mmol), $Na_9[A\text{-}\alpha\text{-}PW_9O_{34}] \cdot 7H_2O$ (0.1 mmol) and KCl (1.00 mmol) were mixed in deionized H_2O (10 mL) in a 25 mL Teflon autoclave and stirred for half an hour, and then the pH value of the mixtures were adjusted to 4.5, 5.5, 6.5, 7.5, 8.5, 9.5 by 1M HCl and 1M NaOH. Then Teflon autoclave was heated to 120 °C for 6 h and then cooling in room temperature and 4 °C overnight successively. The SEM images of preparing $Co_4(PW_9)_2$ microcrystal under different pH, Figure S2 exhibits that merely when pH=7.5 can $Co_4(PW_9)_2$ microcrystal formed.

3.2 Favorable amount of KCl for preparation $Co_4(PW_9)_2$ microcrystal and correspond SEM images

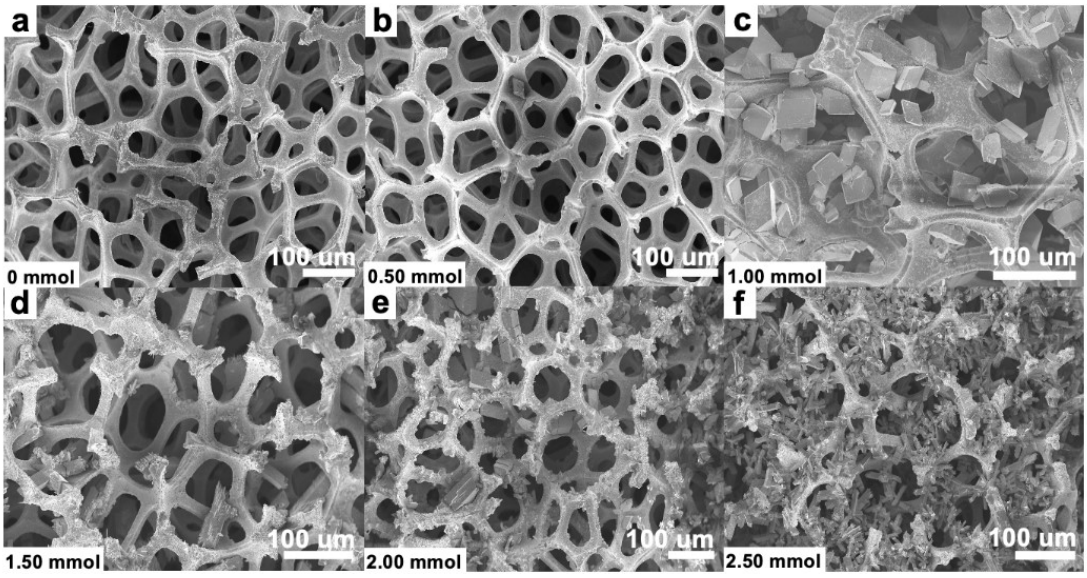

Fig. S3. The SEM images of preparation $Co_4(PW_9)_2$ microcrystal with different amount of KCl

$Co(NO_3)_2 \cdot 6H_2O$ (0.2 mmol), $Na_9[A\text{-}\alpha\text{-}PW_9O_{34}] \cdot 7H_2O$ (0.1 mmol) were mixed in deionized H_2O (10 mL) in a 25 mL Teflon autoclave, then different amount of KCl (0, 0.50, 1.00, 1.50, 2.00 and 2.50 mmol) were added to the mixture. The pH value was fixed at 7.5. After proceeding the same heating and cooling conditions with former, different morphologies of $Co_4(PW_9)_2$ were obtained and observed though SEM in Fig. S3. Only when the amount of KCl added in the mixture is 1.00 mmol, will best morphology of $Co_4(PW_9)_2$ microcrystal be formed.

3.3 ^{1}H-NMR spectrum of HEB-TMS

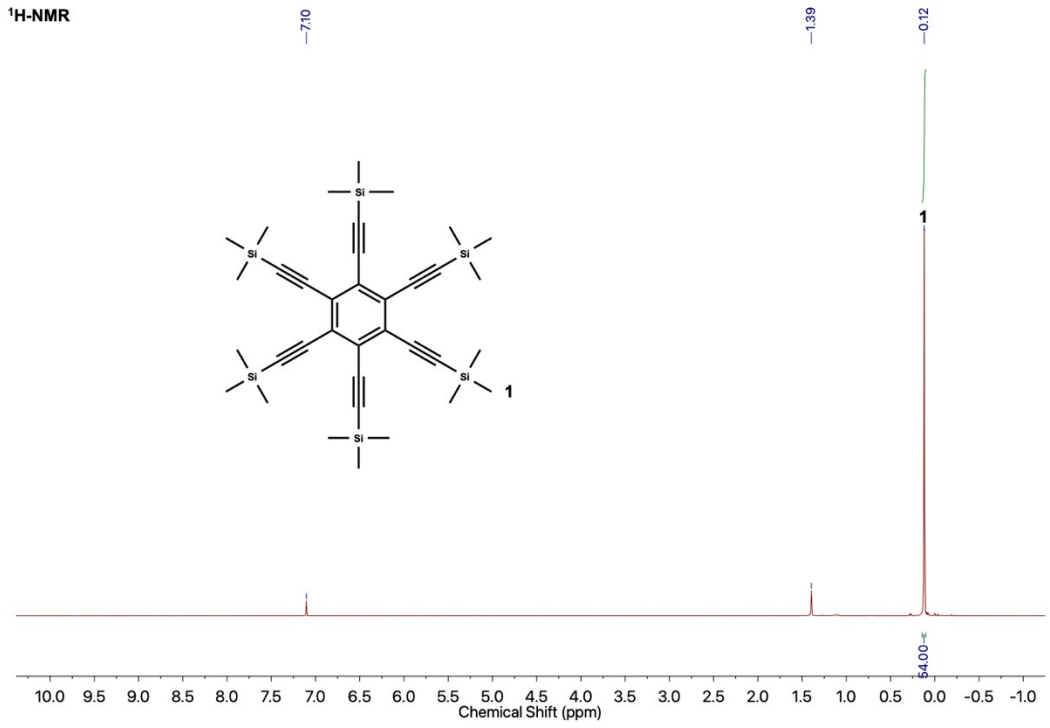

Fig. S4. ^{1}H-NMR spectrum of HEB-TMS

^{1}H NMR (400 MHz, $CDCl_3$) δ 0.12 (s, 54H).

3.4 ^{13}C-NMR spectrum of HEB-TMS

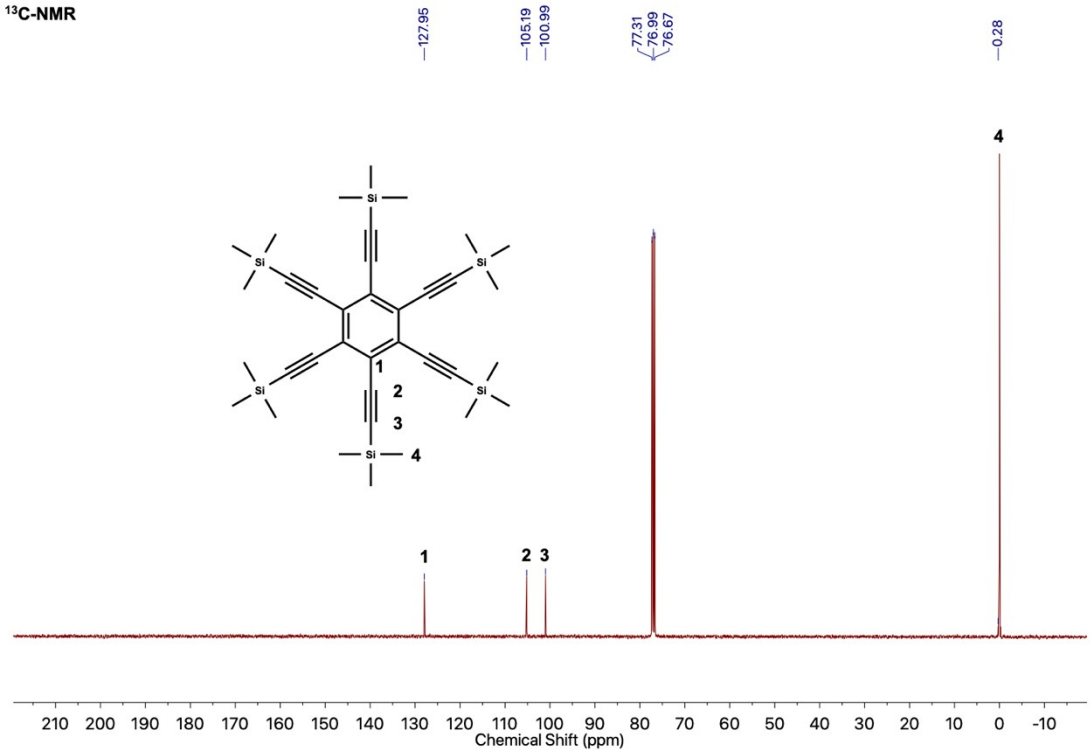

Fig. S5. ^{13}C-NMR spectrum of HEB-TMS

^{13}C NMR (101 MHz, $CDCl_3$) δ 127.95 (C=C), 105.19 (C≡C), 100.99 (C-Si), 0.28 (Si-CH_3).

3.5 Crystallographic data of $Co_4(PW_9)_2$

	$Co_4(PW_9)_2$
formula	$K_{10}[Co_4(PW_9O_{34})_2]\cdot 24H_2O$
Formula weight	5518.34
crystal size[mm^3]	0.25×0.22×0.18
Crystal color	purple
crystal system	monoclinic
space group	P 21/n
a [Å]	12.365 (6)
b [Å]	21.330 (11)
c [Å]	15.827 (8)
α [°]	90
β [°]	92.395 (15)
γ [°]	90
Volume [$Å^3$]	4170 (4)
Z	2
Dcalc. [$mg\cdot m^{-3}$]	4.394
μ[mm^{-1}]	26.145
F_{000}	4888.0
□range[°]	3.206 to 58.996
Reflections collected	42967
Independent reflections	11593
R(int)	0.0710
Completeness	0.998
Data/restraints/parameters	11593/121/616
Goodness-of-fit on F^2	1.020
Final *R* indices [I>2sigma(I)]	R_1 = 0.0370, wR_2 = 0.0923
R indices (all data)	R_1 = 0.0492, wR_2 = 0.0996
Largest diff. peak and hole/e.$Å^{-3}$	3.37/-3.92

Table S1. Crystallographic data and structure refinements

3.6 Thermogravimetric analysis (TGA) of $Co_4(PW_9)_2$

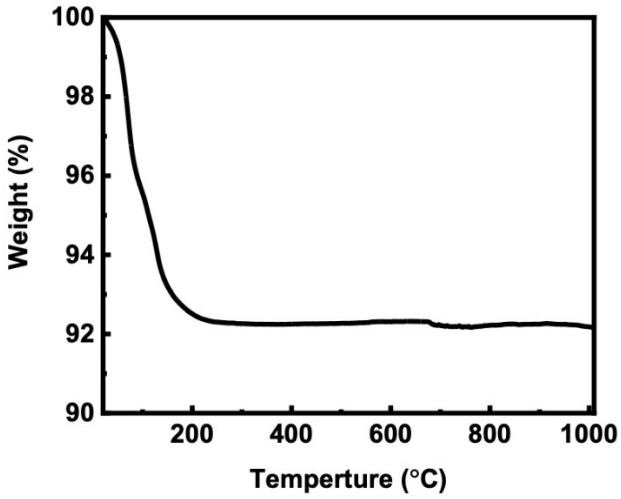

Fig. S6. TGA plot of $Co_4(PW_9)_2$

$Co_4(PW_9)_2$ will lose water molecules under the heating process, the weight loss of $Co_4(PW_9)_2$ is about 8 wt%. From the thermogravimetric curve, we can calculate the loss of water molecules is about 24, to determine the final chemical formula: $K_{10}[Co_4(PW_9O_{34})_2]\cdot 24H_2O$.

3.7 The SEM image of blank CF with porous structure

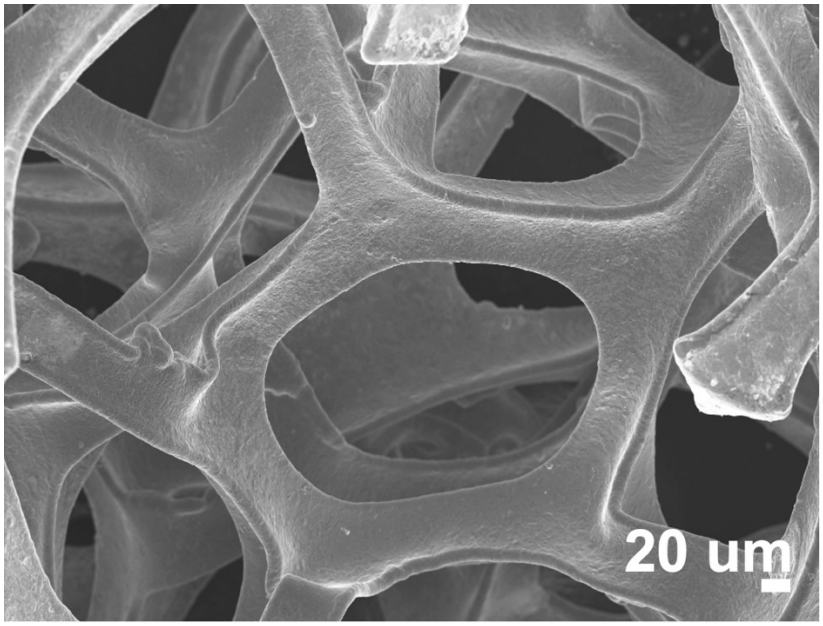

Fig. S7. The SEM image of blank CF

The SEM image in Fig. S7 is bare Co foam for comparison with $Co_4(PW_9)_2$@GDY and $Co_4(PW_9)_2$.

3.8 The EDS elemental mapping of $Co_4(PW_9)_2$@GDY by SEM

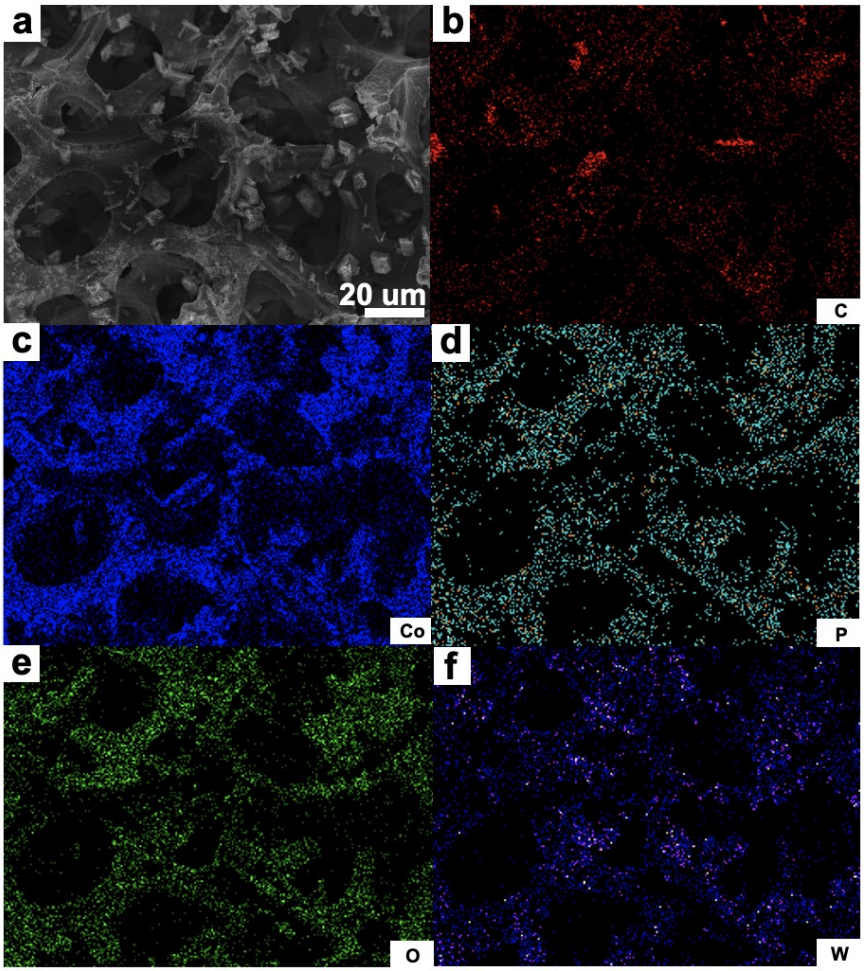

Fig. S8. (a) The SEM image of $Co_4(PW_9)_2$@GDY and corresponding element mapping of (b) C; (c) Co; (d) P; (e) O; (f) W

Fig. S8 shows the uniform distribution of different elements: C, Co, P, O and W in the composite cluster, which proves that $Co_4(PW_9)_2$@GDY was synthesized properly.

3.9 Supplementary of XPS spectrum

3.9.1 Supplementary for $Co_4(PW_9)_2$@GDY

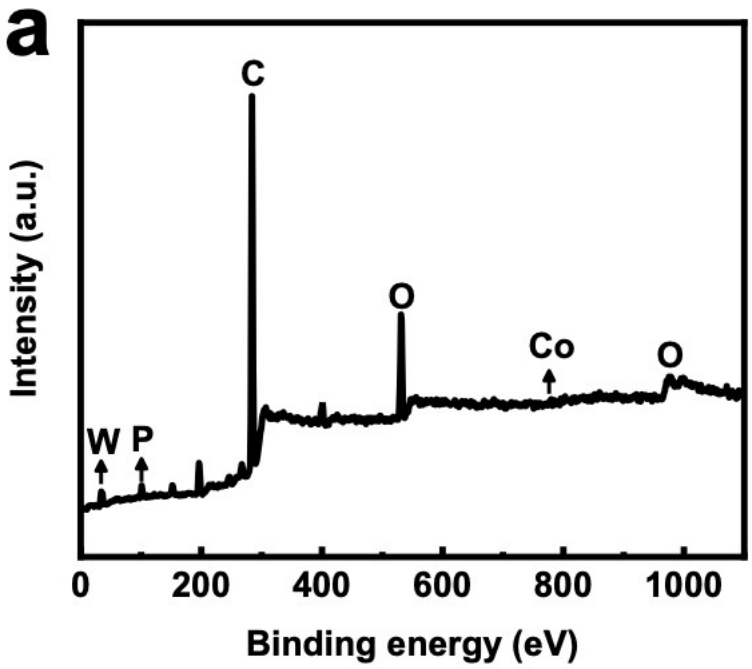

Fig. S9. XPS survey scan of $Co_4(PW_9)_2$@GDY

The XPS survey scan is shown in Fig. S9, which exhibits the presence of W, P, C, O and Co, suggesting the coexistence of $Co_4(PW_9)_2$ and GDY in composite cluster.

3.9.2 Supplementary for $Co_4(PW_9)_2$

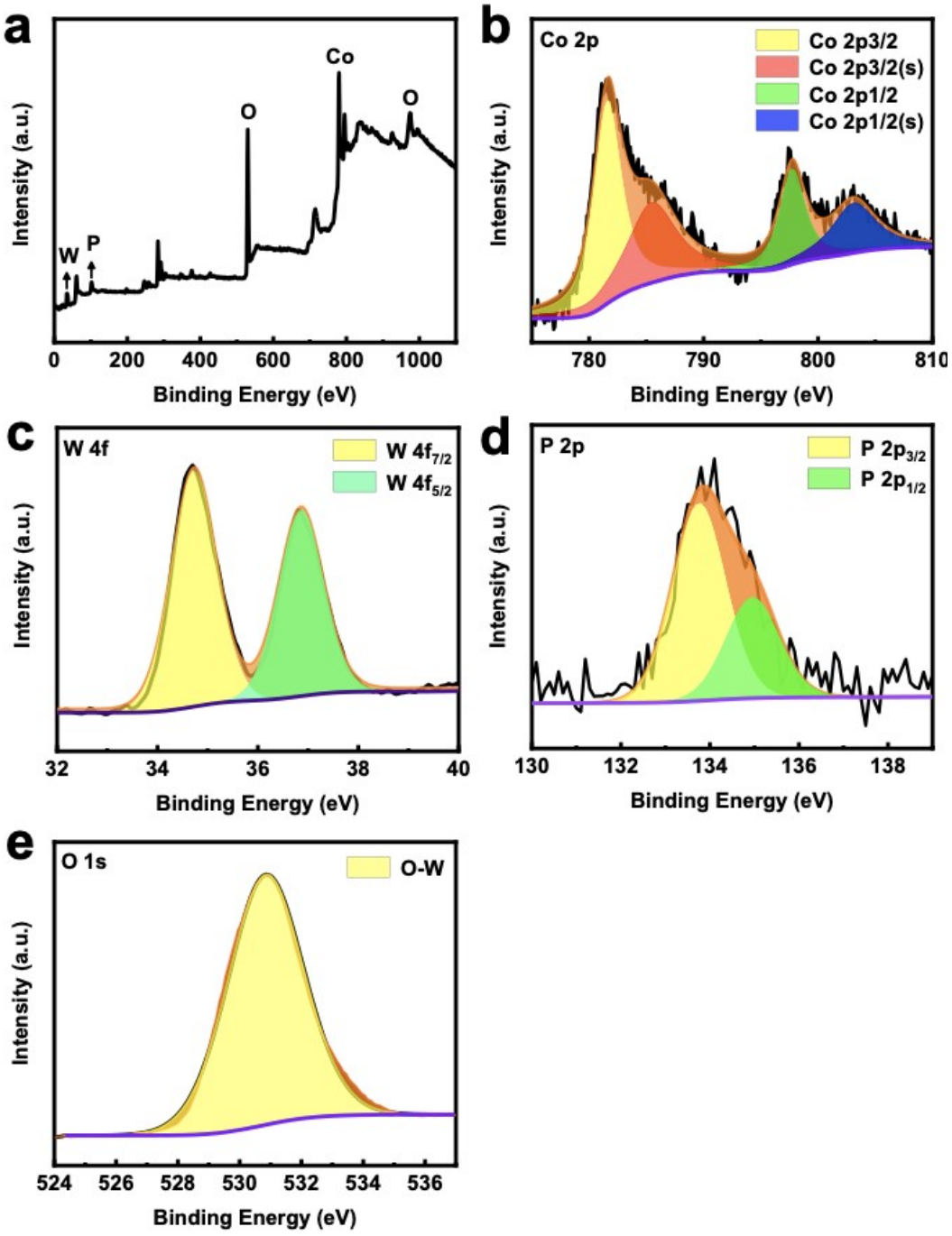

Fig. S10. (a) XPS survey spectrum of $Co_4(PW_9)_2$; high-resolution XPS spectrum of (b) Co 2p, (c) W 4f; (d) P 2p; (e) O 1s in $Co_4(PW_9)_2$

Fig. S10 provides XPS spectrum of $Co_4(PW_9)_2$. Fig. S10a shows the survey scan $Co_4(PW_9)_2$, which exhibits the presence of Co, W, P and O. Fig. S10b shows four main peaks that belong to Co^{2+} (2p), two of them are Co^{2+} $2p_{3/2}$ at 780.4 eV and Co^{2+} $2p_{1/2}$ at

796.1 eV and the others are satellites of Co^{2+} $2p_{3/2}$ and Co^{2+} $2p_{1/2}$ at 786.6 eV and 801.9 eV. Two binding energy at 35.8 eV and 37.0 eV in Fig. S9c could be assigned to W^{6+} $4f_{7/2}$ and W^{6+} $4f_{5/2}$. A doublet induced by spin-orbital coupling can be resolved in Fig. S10d is exclusive for P^{4+} 2p, the corresponding binding energy of P^{4+} $2p_{3/2}$ and P^{4+} $2p_{1/2}$ are 133.7 eV and 134.9 eV. A single peak at 530.8 eV is clearly shown in Fig. S10e which presents the O 1s in O-W bond in $Co_4(PW_9)_2$.

3.9.3 Supplementary for GDY

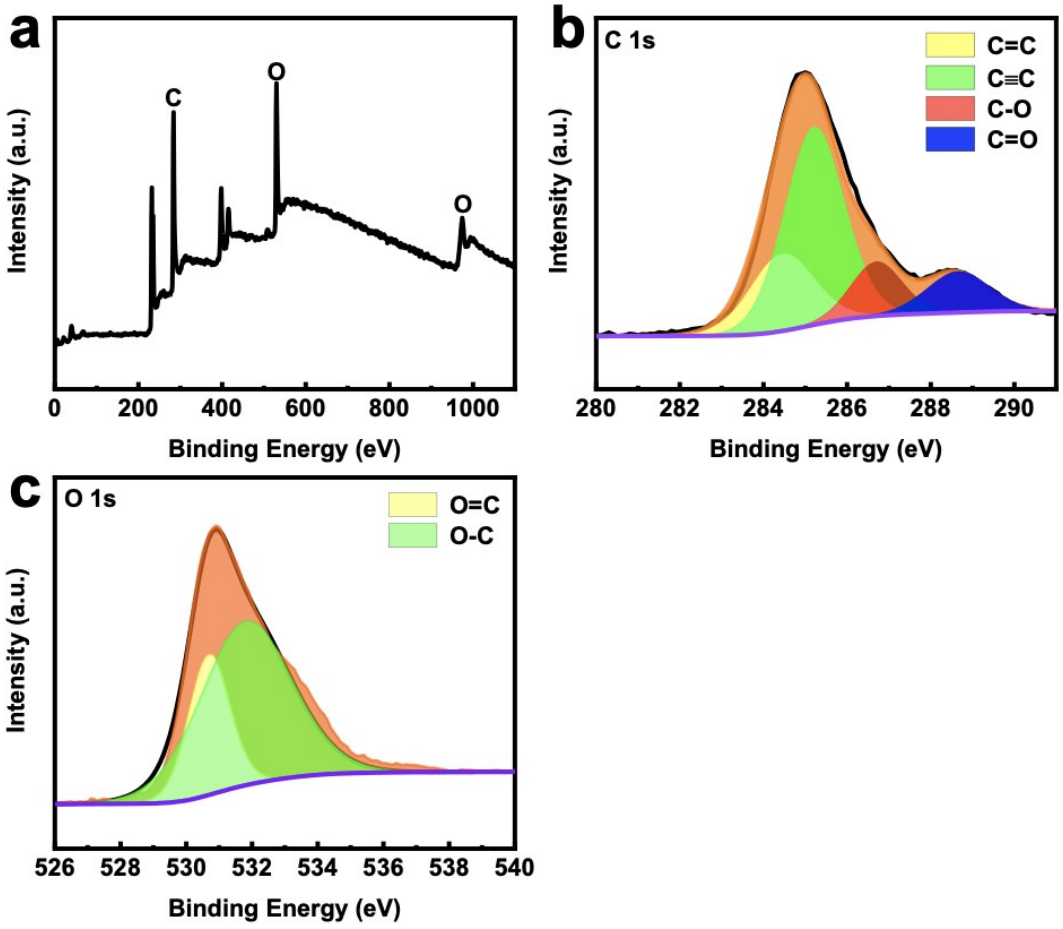

Fig. S11. (a) XPS survey spectrum of GDY; high-resolution XPS spectrum of (b) C 1s, (c) O 1s in GDY

We synthesized the all-carbon GDY individually and the product was also analyzed by XPS. Fig. S11a is XPS survey scan of GDY nanofilm, which exhibits the elements of C (1s) and O (1s). The high-resolution XPS spectra of C 1s in Fig. S11b shows peak at 284.8 eV, which can be deconvolved into four peaks, corresponding to sp^2 (C=C) at binding energy of 284.5 eV, sp (C≡C) at 285.2 eV, C-O at 286.7 eV and C=O at 288.9 eV, respectively. A single peak at 531.1 eV in Fig. S11c could be considered the superposition of two peaks at 530.7 eV and 531.8 eV which accord to O=C and O-C, respectively. The formation for single bond and double bond between Carbon and Oxygen are believed to be the adsorption of air. It is worth noting that the area of pale-

yellow section dwindles obviously in Fig. S11c when compared with Fig. 5f, which can be attributed to the similar binding energy of O 1s in O-W and in O=C, this result can also demonstrate the formation of W-O bond, futher proof that $Co_4(PW_9)_2$ was well prepared.

3.9.4 Supplementary for $Co_4(PW_9)_2$@GDY-after cycling

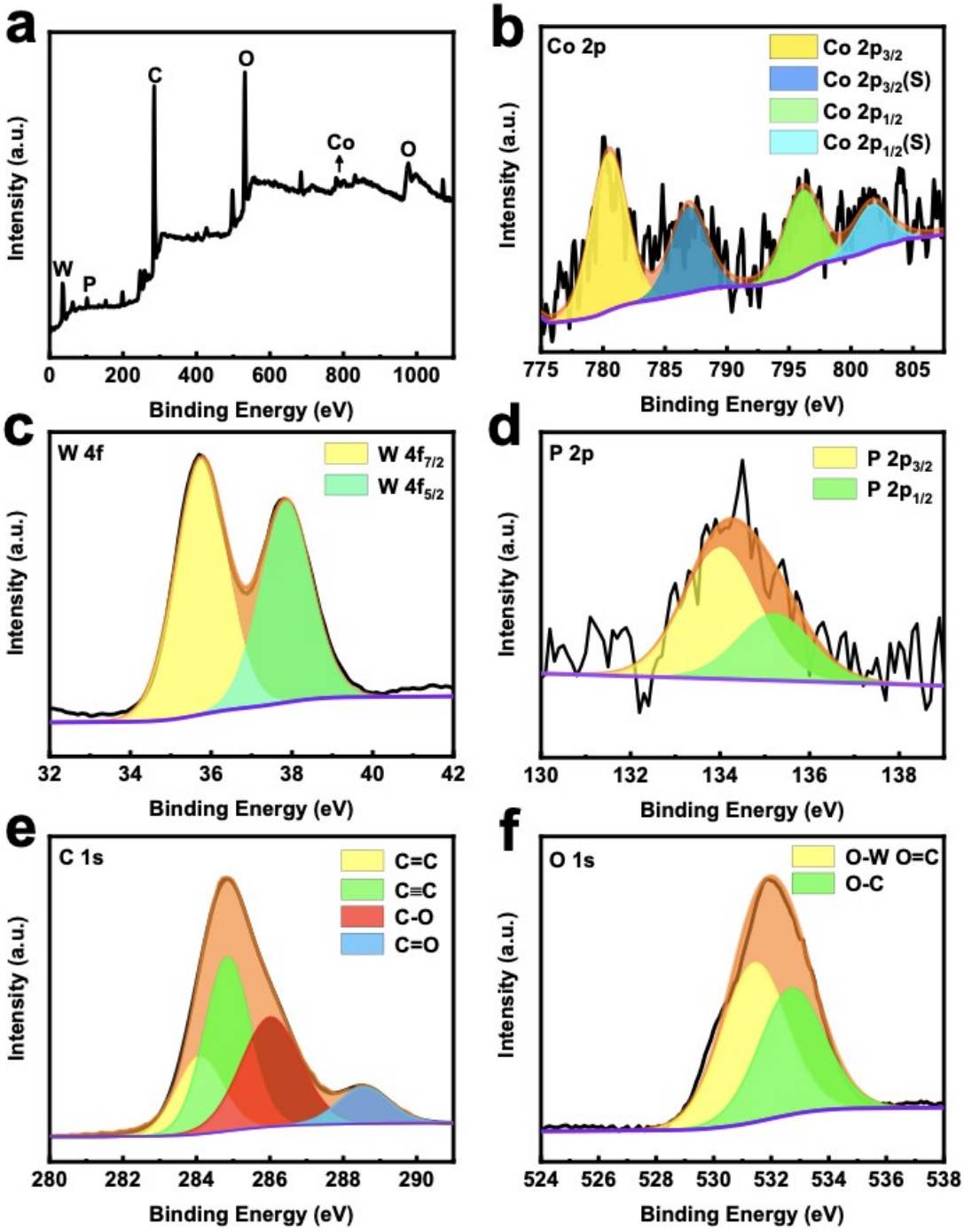

Fig. S12. (a) XPS survey spectrum of $Co_4(PW_9)_2$@GDY-after cycling; high-resolution XPS spectrum of (b) Co 2p, (c) W 4f, (d) P 2p, (e) C 1s and (f) O 1s in $Co_4(PW_9)_2$@GDY-after cycling

The composite electrode of $Co_4(PW_9)_2$@GDY were taken out of the cell and washed by ethanol in ultrasonic condition after cycling, the $Co_4(PW_9)_2$@GDY composite cluster fell from electrode was gathered and collected for XPS measurement. The results are shown in Fig. S12a, the survey scan of $Co_4(PW_9)_2$@GDY-after cycling shows the elements of W, P, C, O and Co and the binding energy of each element basically consistent with $Co_4(PW_9)_2$@GDY before cycling (Fig. S9), which represents the structural integrity of composite cluster was not destroyed during OER, suggesting the excellent electrochemical stability of $Co_4(PW_9)_2$@GDY.

Four characteristic peaks in Fig. S12b could be ascribed to Co^{2+} 2p. The binding energy of Co^{2+} $2p_{3/2}$ and its satellite are 781.2 eV and 785.8 eV, the binding energy of Co^{2+} $2p_{1/2}$ and its satellite are 797.3 eV and 802.7 eV. Peak exhibited in Fig. S12c could be resolved into W^{6+} $4f_{7/2}$ and W^{6+} $4f_{5/2}$ doublets and their corresponding binding energy are 35.5 eV and 37.7 eV. Similarly, two signals could be observed in Fig. S12d at 133.9 eV and 135.1 eV which could be assigned to P^{4+} $2p_{3/2}$ and P^{4+} $2p_{1/2}$. Fig. S12e depicts a peak at 284.9 eV, and it can be deconvolved into sp^2 (C=C) at binding energy of 284.1 eV, sp (C≡C) at 284.9 eV, C-O at 286.0 eV and C=O at 288.6 eV. Finally, Fig. S12f illustrates a single peak at 531.9 eV and its resolved peaks are O-W and O=C at 531.4 eV, O-C at 532.7 eV.

3.10 Cyclic voltammetry (CV) curve for different electrodes

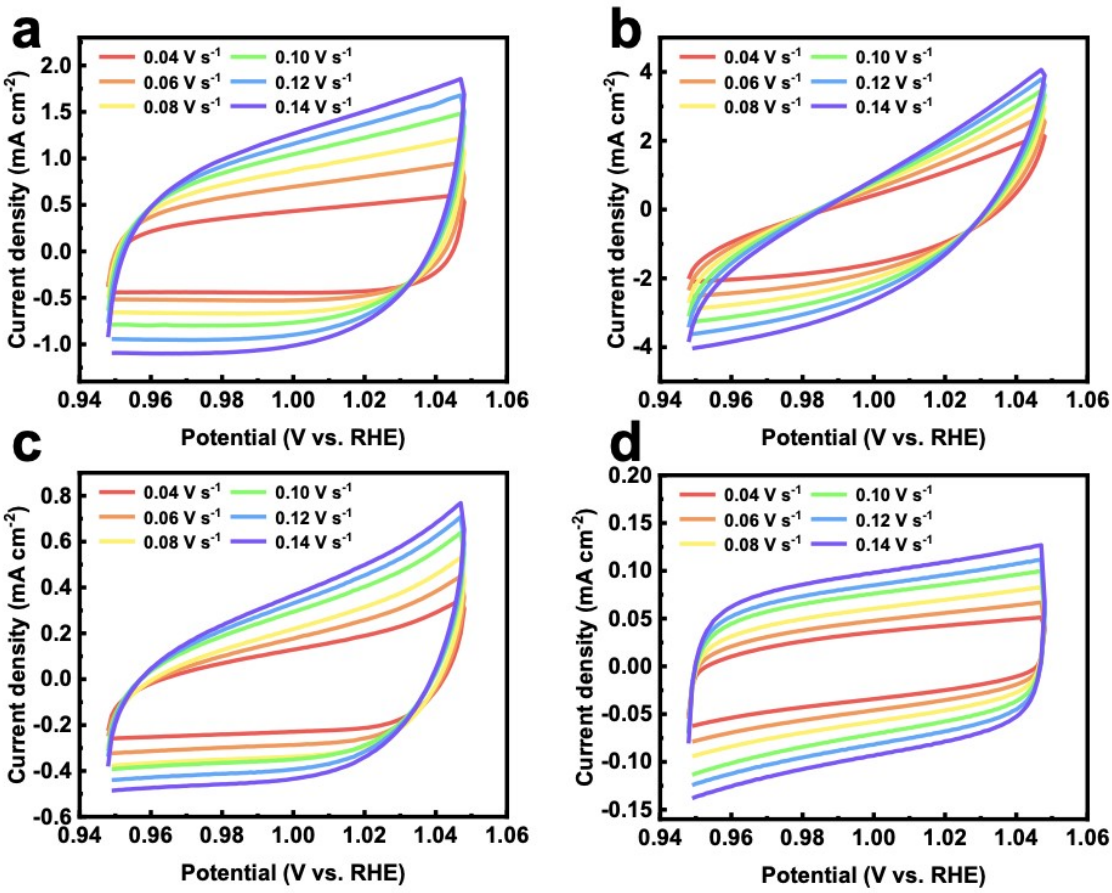

Fig. S13. CV curves of (a) $Co_4(PW_9)_2$@GDY, (b) $Co_4(PW_9)_2$, (c) GDY and (d) CF in the potential range of 0.96-1.04 V vs RHE at various scan rates (40-140 mV s^{-1}).

The CV curves in Fig. S13 of four electrodes are used for plotting the graphs of current density against the scan rate to calculate the C_{dl} at potential of 1.02 V (vs. RHE) in Fig. 6c. The ECSA of the catalyst was estimated from the electrochemical double-layer capacitance (C_{dl}). C_{dl} was measured via CV curve with a potential range where no apparent Faradaic process was taking place. The double-layer charging current I_C can be related to the scan rates through Equation S1:

$$I_C = C_{dl} \times v \quad \text{(Equation S1)}$$

Thus, plotting the charge current at a specific potential against various scan rates yields a straight line which slope is equal to C_{dl}. Subsequently, the ECSA can be obtained by Equation S2:

$$ECSA = \frac{C_{dl}}{C_S} \quad \text{(Equation S2)}$$

where C_S is specific capacitance measured from ideally smooth, planar surfaces of the catalyst, the C_S value is 0.04 mF cm^{-2} in 1 M KOH based on the typical reported values.[6]

3.11 Supplementary for TOF

	$Co_4(PW_9)_2$@GDY	$Co_4(PW_9)_2$
Qredox in CV [C]	0.018	0.009
Moles of active sites [mol cm^{-2}]	9.32×10^{-8}	4.66×10^{-8}
Total number of active sites [cm^{-2}]	5.61×10^{16}	2.80×10^{16}
Current density at η = 350 mV [mA cm^{-2}]	31.00	11.47
TOF value at η = 350 mV [s^{-1}]	0.86	0.63

Table S2. TOF and relevant parameters of composite electrode at overpotential 350 mV

The turnover frequency (TOF) was determined to better explore the intrinsic activity of the $Co_4(PW_9)_2$@GDY and $Co_4(PW_9)_2$ in the OER by using the approach of redox peak integration of CV in static solution, which was calculated from the expression:

$$TOF = \frac{j \times S}{2 \times Q_{redox}} \quad \text{(Equation S3)}$$

where j is current density at a certain overpotential, S is the area of nanocomposite electrode and Q_{redox} is the Faradaic charges when redox reaction occurs of the active sites and is calculated by the redox peaks under the baseline-corrected cyclic voltammetry.

3.12 SEM images of $Co_4(PW_9)_2$@GDY after cycling

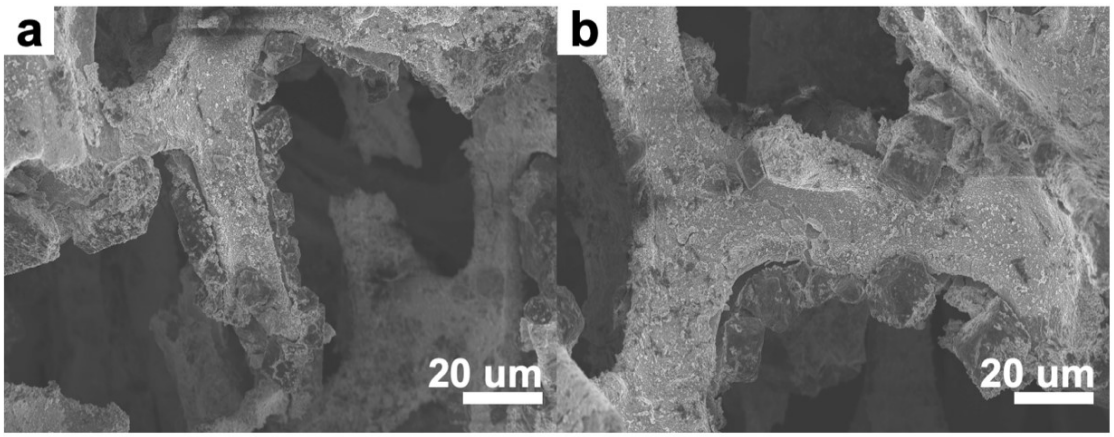

Fig. S14. (a) and (b) are the SEM images of $Co_4(PW_9)_2$@GDY-after OER cycling.

As shown in Fig. S14a and Fig. S14b, the morphology of $Co_4(PW_9)_2$@GDY after OER cycling unchanged which provides a joint proof with PXRD patterns in Fig. 6f that the $Co_4(PW_9)_2$@GDY electrode possesses relatively high stability and robustness.

3.13 Raman spectrum of $Co_4(PW_9)_2$@GDY after cycling

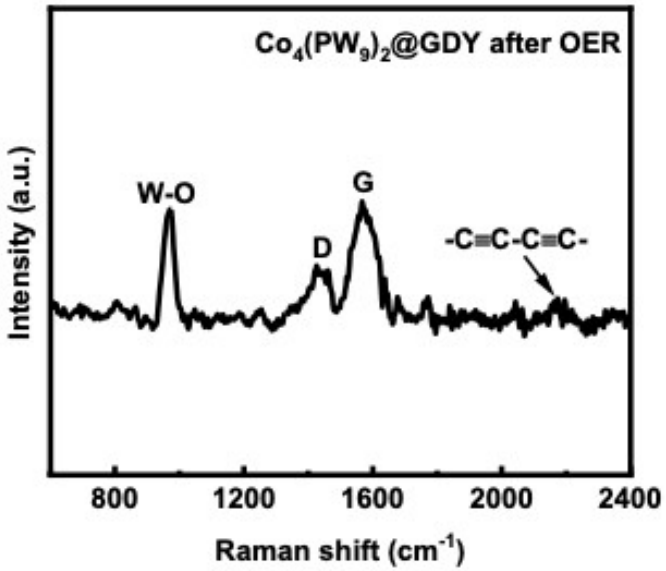

Fig. S15. Raman spectrum of $Co_4(PW_9)_2$@GDY after OER cycling.

As shown in Fig. S15, the Raman result of $Co_4(PW_9)_2$@GDY after OER suggesting the excellent electrochemical stability of composite cluster.

3.14 EIS and relating results

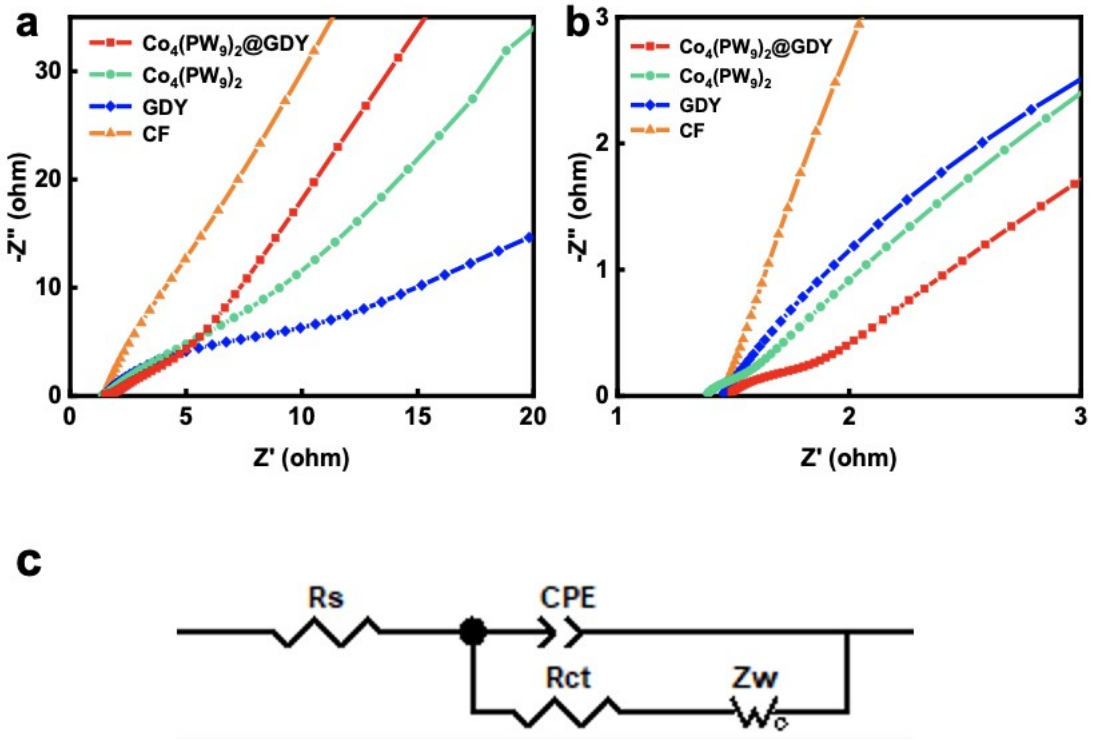

Fig. S16. (a) and (b) are Nyquist plots of the $Co_4(PW_9)_2$@GDY, $Co_4(PW_9)_2$, GDY and CF in different scale; (c) the equivalent circuit model used for fitting

	R_s (Ω)	R_{ct} (Ω)
$Co_4(PW_9)_2$@GDY	1.49	0.70
$Co_4(PW_9)_2$	1.38	6.66
GDY	1.44	16.06
Co foam	1.46	73.08

Table S3. R_s and R_{ct} value of $Co_4(PW_9)_2$@GDY, $Co_4(PW_9)_2$, GDY and Co foam

3.15 ICP-OES results

ICP-OES was conducted to determine the content of Co, P, W in $Co_4(PW_9)_2$ clusters, which were removed from the CF by ultrasonic. The element content could be found in Table S4. The ratio of Co, P, W is close to 4:2:18, corresponding to the ratio of content in $Co_4(PW_9)_2$ formula.

Table S4. ICP-OES result for $Co_4(PW_9)_2$

elements	$Co_4(PW_9)_2$
Co	4.66%
P	2.23%
W	21.97%

3.16 EDS elemental analysis

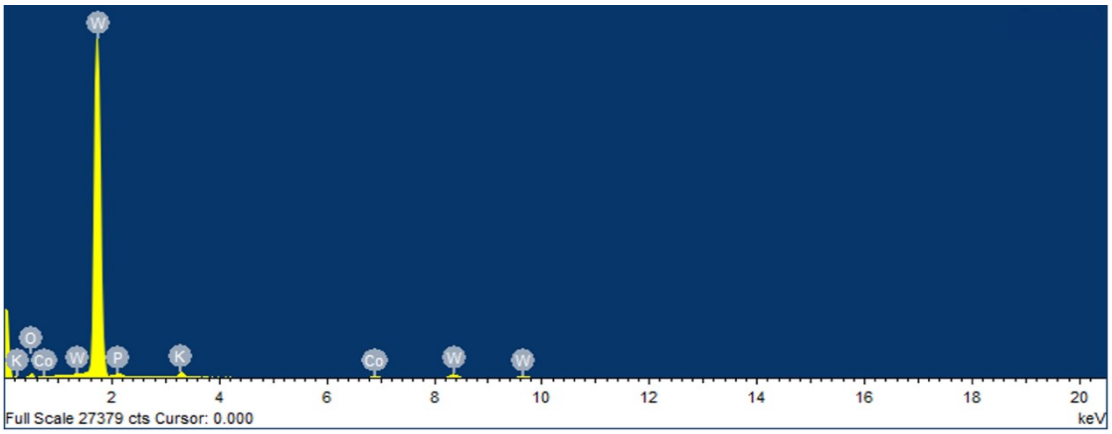

The elemental analysis results of $Co_4(PW_9)_2$ are shown in Fig. S16-S17 and Table S5.

Fig. S17. Elemental analysis of $Co_4(PW_9)_2$

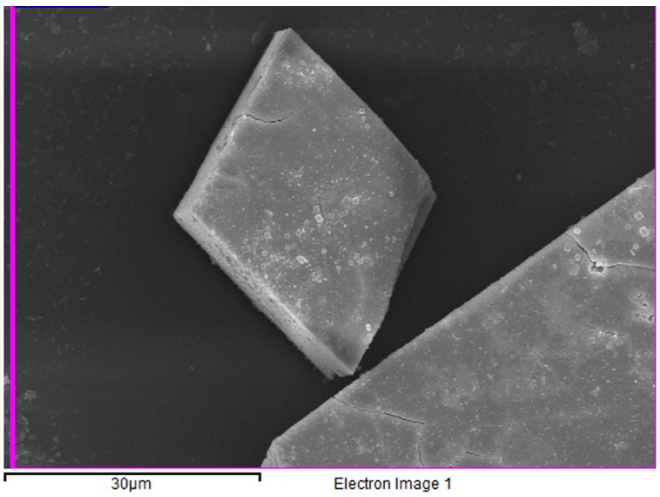

Fig. S18. Selected area of $Co_4(PW_9)_2$ for EDS

\

Table S5 element content in $Co_4(PW_9)_2$

Element	Weight%	Atomic%
O K	18.67	64.22
P K	1.21	2.19
K K	7.33	9.80
Co K	5.12	4.54
W L	67.67	19.25
Total	100	100

The EDS results as shown in Table S5, the element ratio and content of different are cosistent with $Co_4(PW_9)_2$.

The elemental analysis results of $Co_4(PW_9)_2$@GDY are shown in Fig. S18-S19 and Table S6.

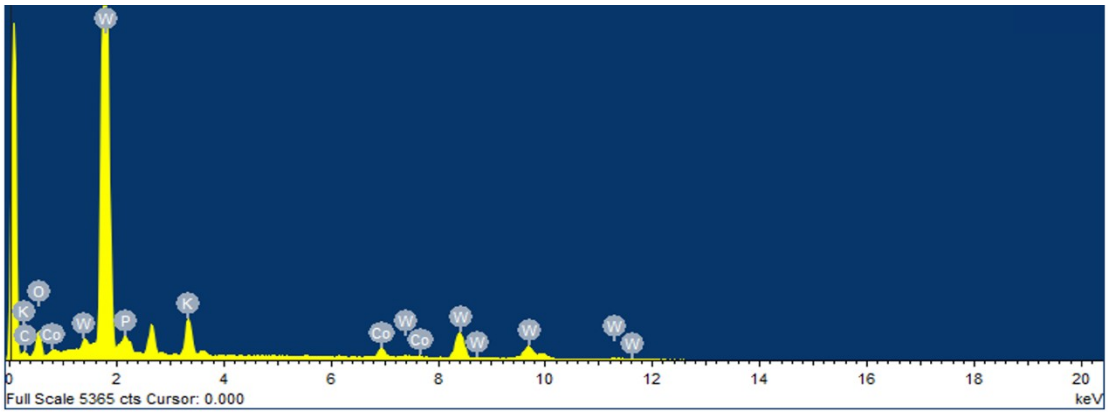

Fig. S19. Elemental analysis of $Co_4(PW_9)_2$@GDY

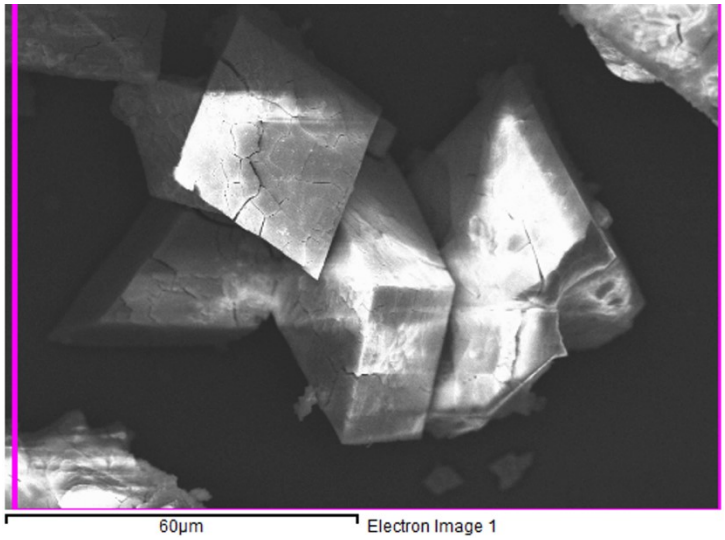

Fig. S20. Selected area of $Co_4(PW_9)_2$@GDY for EDS

Table S6 element content in $Co_4(PW_9)_2$@GDY

Element	Weight%	Atomic%
C K	0.33	1.43
O K	18.46	63.34
P K	1.12	2.03
K K	8.83	10.33
Co K	4.85	4.24
W L	66.41	18.63
Total	100	100

The EDS results as shown in Table S5 exhibit that the C content of $Co_4(PW_9)_2$@GDY is 1.43%.

3.17 Faraday efficiency (FE)

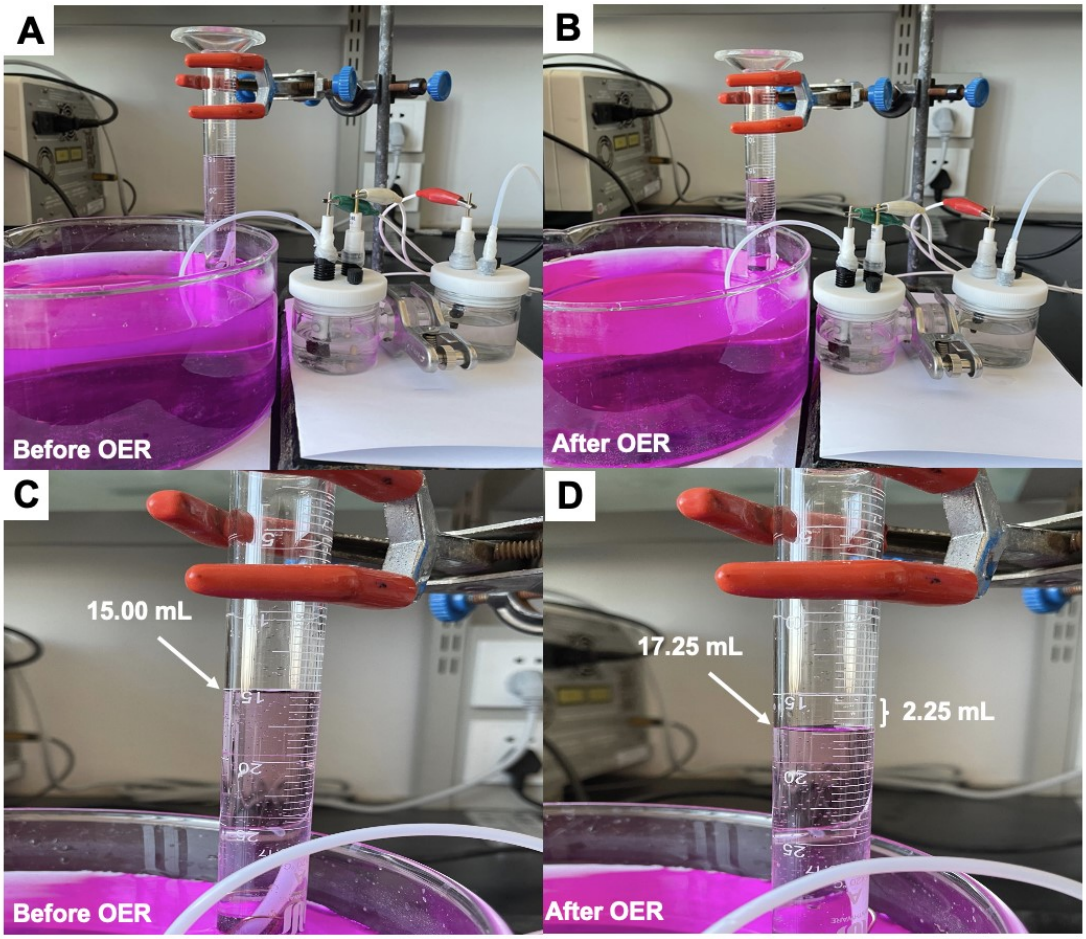

Fig. S21. (a) and (b) are H-cell and drainage and gas storage device before and after OER; (c) and (d) are partical magnification images that shows clearly about the scale of graduated cylinder before and after OER

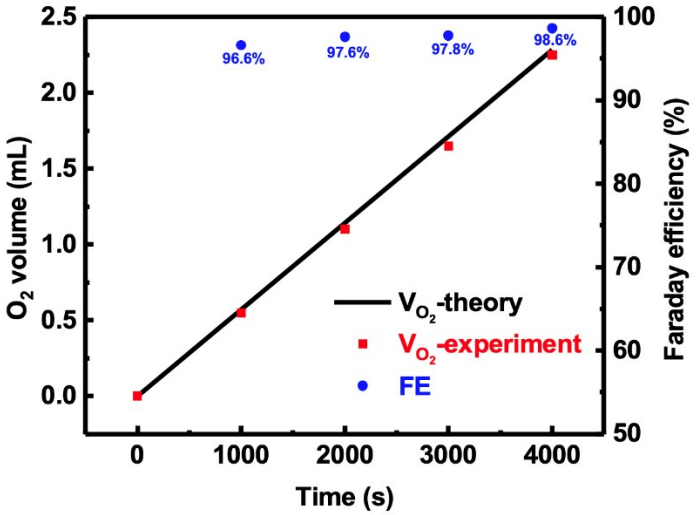

Fig. S22. The volume of O_2 of experiment and theory, and corresponding Faraday efficiency at different time points.

FE were calculated according to the Equation S4-1 and Equation S4-2

$$FE = \frac{V(O_2 - experient)}{V(O_2 - theory)} \quad \text{(Equation S4-1)}$$

$$V(O_2 - theory) = \frac{Q_t}{4 \times F} \times V_m \times \frac{298K}{273K} \quad \text{(Equation S4-2)}$$

$V(O_2\text{-experiment})$ were recorded at different time point (1000s, 2000s, 3000s and 4000s); Q_t is total charges at different time point, which was calculated according to the i-t curve from electrochemical workstation; F is Faraday constant, F=96485 C/mol; V_m is gas molar volume, V_m=22.4 L/mol.

3.18 DFT calculation and model

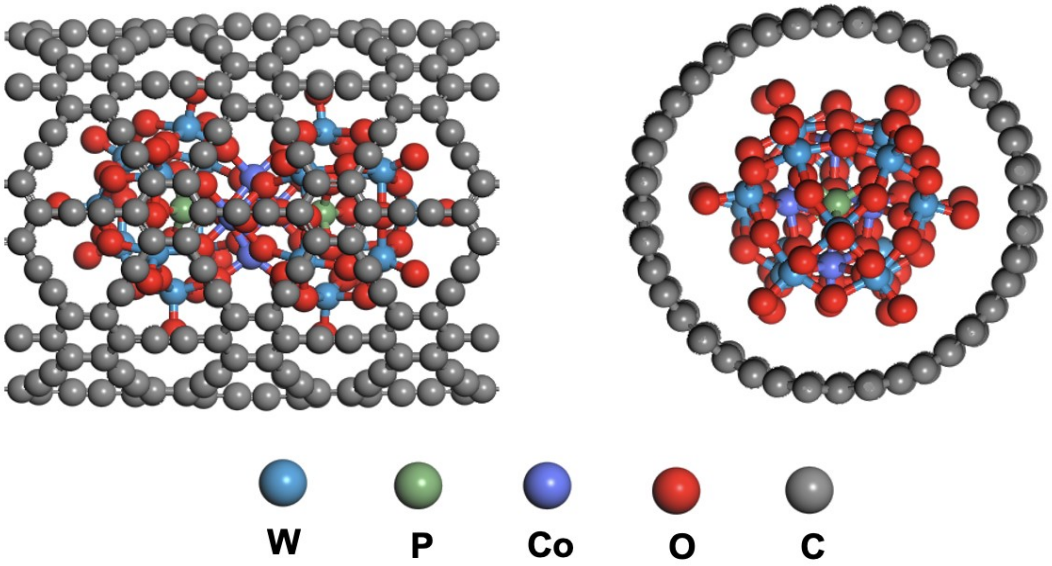

Fig. S23. The calculation model of $Co_4(PW_9)_2$@GDY, the monomer $Co_4(PW_9)_2$ was encapsulated in GDY tube

For $Co_4(PW_9)_2$@GDY, a monomer of $Co_4(PW_9)_2$ structure is encapsulated by a GDY tube (shown in Fig. S18). A vacuum layer as large as 12 Å was used along the direction of the surface normal to avoid periodic interactions. In all structural optimization calculations, all the atoms were allowed to relax. A vacuum layer as large as 10 Å was used along a and c directions to avoid periodic interactions.

The electrode is working under the potential in reality. To investigate the effect of the electric potential on the activity of OER, the free energy diagrams of OER is employed.[3] Free energy change from initial states to final states of the reaction is calculated as follows:

$$\Delta G = \Delta E + \Delta ZPE - T\Delta S + \Delta G_U + \Delta G_{pH} \quad \text{(Equation S5)}$$

where ΔE is the total energy change based on the DFT calculations, ΔZPE and ΔS is the change in zero-point energy and in entropy, respectively, T is room temperature (298.15 K). ΔG_U=-eU, where U is the electrode potential with respect to standard

hydrogen electrode, and *e* is the transferred charge. Since the results of the free energy diagrams are consistent in both pH = 0 and pH = 14.[2] Thus, free energy change of pH ($\Delta G_{pH} = k_B T \ln 10 \times pH$ where k_B is the Boltzmann constant) only employ the configuration of pH = 0 in this work. The free energy of H_2O was estimated in the gas-phase with a pressure of 0.035 bar, which is the equilibrium vapor pressure of H_2O at 298.15 K. The free energy of O_2 is obtained from the free energy change of the reaction $O_2 + 2H_2 \rightarrow 2H_2O$, which is -4.92 eV at 298.15 K and a pressure of 0.035 bar. The free energy of $(H^+ + e^-)$ at standard conditions was assumed as the energy of $1/2H_2$.[4] The entropy of the H_2 is taken from the NIST database, while the entropies of the OER intermediates were calculated from the vibrational frequencies.

3.19 Working potential to active sites in pure GDY

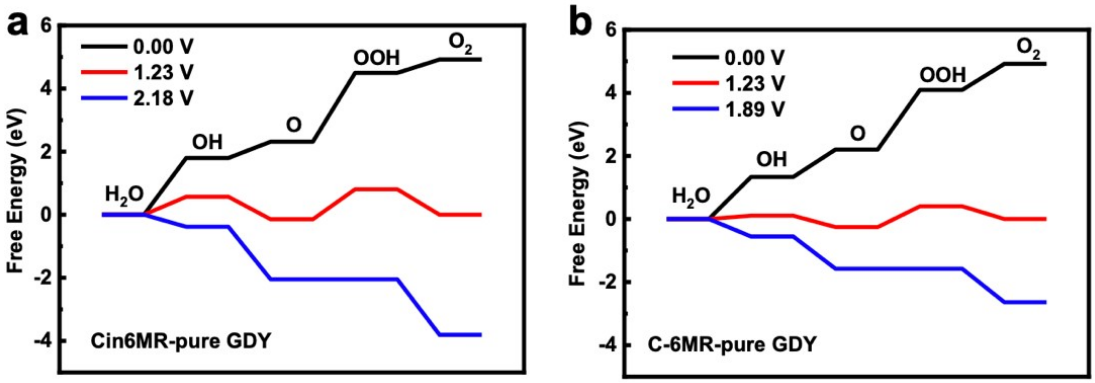

Fig. S24. The calculation model of $Co_4(PW_9)_2$@GDY, the monomer $Co_4(PW_9)_2$ was encapsulated in GDY tube.

As shown in Figure S21, the applied working potential of Cin6MR and C-6MR in pure GDY is 2.18 V and 1.89 V (vs. RHE), which are higher than the same active sites in $Co_4(PW_9)_2$@GDY, Cin6MR for 2.13 V, Cin6MR' for 2.01 V and C-6MR for 1.78 V (vs. RHE).

Table S7. The free energy changes (in eV) for elementary reactions in OER with external potential of 0 V. The values in red indicates the potential-limiting step.

	C-6MR-$Co_4(PW_9)_2$@GDY	Cin6MR-$Co_4(PW_9)_2$@GDY	Cin6MR'-$Co_4(PW_9)_2$@GDY
H_2O → *OH	1.14	1.69	1.45
*OH → *O	0.91	0.59	0.69
*O → *OOH	1.78	2.13	2.01
*OOH → O_2	1.09	0.51	0.76

3.20 Comparison for different active sites

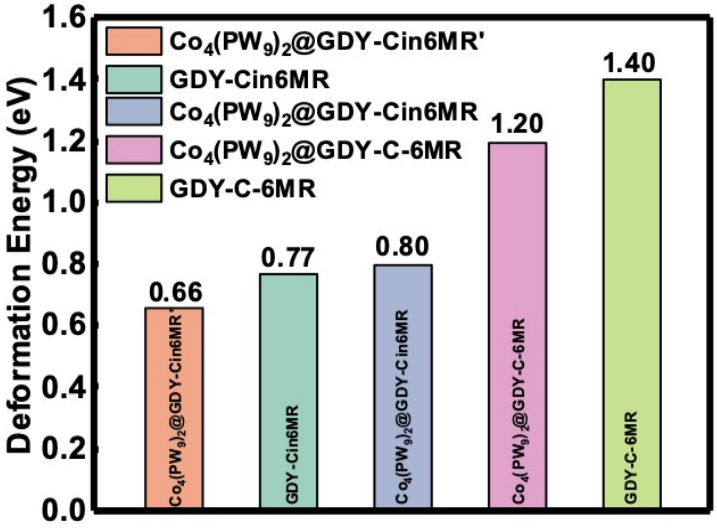

Fig. S25. Comparison of deformation energy for C-6MR, Cin6MR and Cin6MR' active sites in $Co_4(PW_9)_2$@GDY and C-6MR, Cin6MR active sites in GDY.

3.21 Images of different electrodes under optical microscope

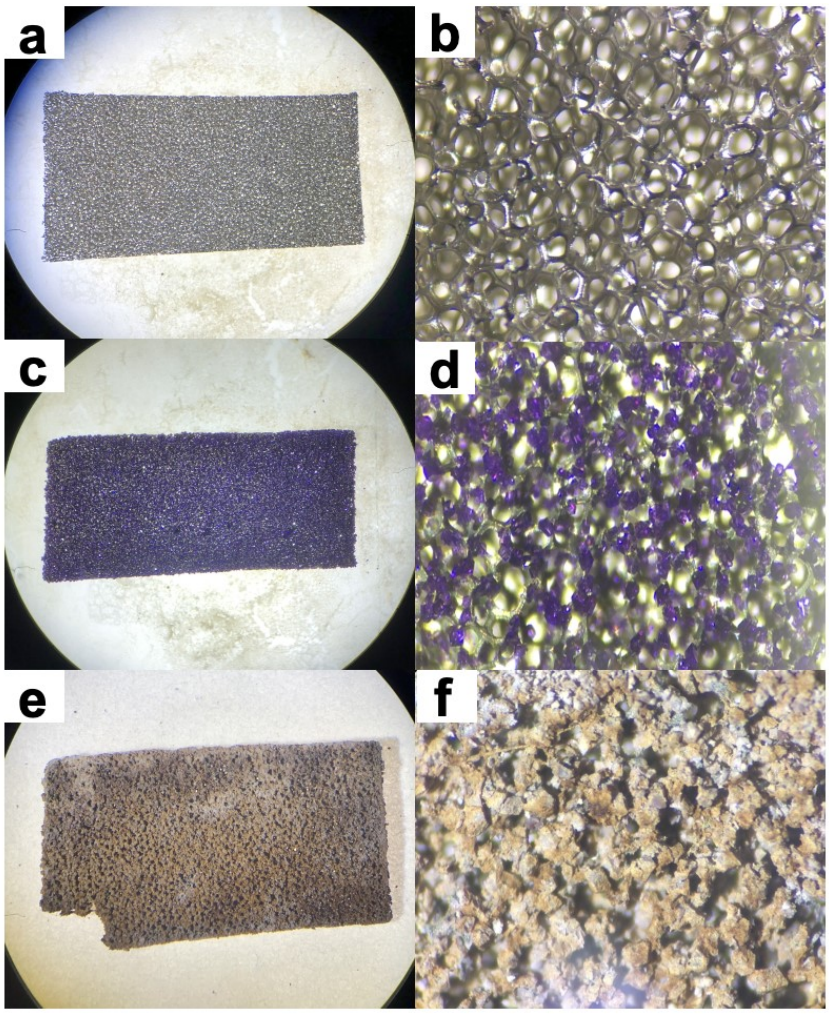

Fig. S26. (a) and (b) are the images of blank Co foam under the optical microscope; (c) and (d) are the images of $Co_4(PW_9)_2$ microcrystal deposited in Co foam under the optical microscope; (e) and (f) are the images of core-shell structure of $Co_4(PW_9)_2$@GDY loaded on Co foam under the optical microscope.

3.22 Comparsion of OER performance

Table S8. Literature survey on potential and Tafel slope of the Co-based nanostructures for OER.

Electrocatalysts	**Electrolyte**	***j* *[mA cm^{-2}]***	**potential (V *vs* RHE)**	**Tafel slop (mV dec^{-1})**	**References**
$Co_4(PW_9)_2$@ GDY/CF	1.0 M KOH	10 20 50 100 200	1.52 1.56 1.59 1.62 1.66	80	*this work*
Wire-like MoS_2/Fe-$NiCo_2O4$	1.0 M NaOH	10	1.54	42	*5*
$[Co_{6.8}Ni_{1.2}W_{12}O_{42}(OH)_4(H_2O)_8]$	0.1 M KOH	10	1.59	126	*6*
CoO/Co_3O_4	1.0 M KOH	10	1.50	55	*7*
Co_3O_4/N-graphene	1.0 M KOH	10	1.54	67	*8*
CoNi1@C	1.0 M KOH	10	1.57	55	*9*
$NiCo_2O_4$@MnO_2	1.0 M	10	1.57	89	*10*

core-shell nanoarray	KOH				
$NiCo_2O_4$/rGO	0.1 M KOH	10	1.68	53	*11*
$NiCo_2O_4$/NiO nanosheets	1.0 M KOH	10	1.60	61	*12*
CoP/MoP@NC	1.0 M KOH	10	1.50	81	*13*
Fe-$NiCo_2O_4$ nanowire	1.0 M KOH	10	1.58	27	*14*

References

[1] G. Li, Y. Li, H. Liu, Y. Guo, Y. Li, D. Zhu, *Chem. Commun.*, 2010, **46**, 3256.

[2] M. Sonoda, A. Inaba, K. Itahashi, Y. Tobe, *Org. Lett.*, 2001, **3**, 2419.

[3] J. K. Nørskov, J. Rossmeisl, A. Logadottir, L. Lindqvist, J. R. Kitchin, T. Bligaard, H. Jónsson, *J. Phys. Chem. B*, 2004, **108**, 17886.

[4] M. Jiao, W. Song, K. Li, Y. Wang, Z. J. Wu, *J. Phys. Chem. C*, 2016, **120**, 8804.

[5] J. Li, D. Chu, H. Dong, D. R. Baker, R. Jiang, *J. Am. Chem. Soc.*, 2020, **142**, 50.

[6] W. Luo, J. Hu, H. Diao, B. Schewarz, C. Streb. Y. F. Song, *Angew. Chem. Int. Ed.*, 2017, **56**, 4941.

[7] D. He, X. Song, W. Li, C. Tang, J. Liu, Z. Ke, C. Jiang, X. Xiao, *Angew. Chem. Int. Ed.*, 2020, **132**, 6996.

[8] Y. Liang, Y. Li, H. Wang, J. Zhou, J. Wang, T. Regier, H. Dai, *Nat. Mater.*, 2011, **10**, 780.

[9] X. Zhang, J. Luo, K. Wan, D. Plessers, B. Sels, J. Song, L. Chen, T. Zhang, P. Tang, J. R. Morante, J. Arbiol, J. Fransaer, *J. Mater. Chem. A*, 2019, **7**, 1616.

[10] H. Xue, H. Yu, Y. Li, K. Deng, Y. Xu, X. Li, H. Wang, L. Wang, *Nanotechnology*, 2018, **29**, 22085401.

[11] E. Umeshbabu, G. Rajeshkhanna, P. Justin, G. R. Rao, *J. Soild State Electrochem.*, 2016, **20**, 2725.

[12] C. Mahala, M. Basu, *ACS Omega*, 2017, **2**, 7559.

[13] Y. J. Tang, H. J. Zhu, L. Z. Dong, A. M. Zhang, S. L. Li, J. Liu, Y. Q. Lan, *Appl. Catal. B-Environ.*, 2019, **245**, 528.

[14] K. L. Yan, X. Shang, Z. Li, B. Dong, X. Li, W. K. Gao, J. C. Chi, Y. M. Chai, C. G. Liu, *Appl. Surface Sci.*, 2017, **416**, 371.